Daily Rainfall Estimate by Emissivity Temporal Variation from 10 Satellites

YALEI YOU,[a,b] S. JOSEPH MUNCHAK,[c] CHRISTA PETERS-LIDARD,[c] AND SARAH RINGERUD[b,c]

[a] *Cooperative Institute for Satellites Earth System Studies, University of Maryland, College Park, College Park, Maryland*
[b] *Earth System Science Interdisciplinary Center, University of Maryland, College Park, College Park, Maryland*
[c] *NASA Goddard Space Flight Center, Greenbelt, Maryland*

(Manuscript received 1 August 2020, in final form 24 December 2020)

ABSTRACT: Rainfall retrieval algorithms for passive microwave radiometers often exploit the brightness temperature depression due to ice scattering at high-frequency channels (≥85 GHz) over land. This study presents an alternate method to estimate the daily rainfall amount using the emissivity temporal variation (i.e., Δe) under rain-free conditions at low-frequency channels (19, 24, and 37 GHz). Emissivity is derived from 10 passive microwave radiometers, including the Global Precipitation Measurement (GPM) Microwave Imager (GMI), the Advanced Microwave Scanning Radiometer 2 (AMSR2), three Special Sensor Microwave Imager/Sounders (SSMIS), the Advanced Technology Microwave Sounder (ATMS), and four Advanced Microwave Sounding Units-A (AMSU-A). Four different satellite combination schemes are used to derive the Δe for daily rainfall estimates. They are all 10 satellites, 5 imagers, 6 satellites with very different equator crossing times, and GMI only. Results show that Δe from all 10 satellites has the best performance with a correlation of 0.60 and RMSE of 6.52 mm, compared with the Integrated Multisatellite Retrievals for GPM (IMERG) Final run product. The 6-satellites scheme has comparable performance with the all-10-satellites scheme. The 5-imagers scheme performs noticeably worse with a correlation of 0.49 and RMSE of 7.28 mm, while the GMI-only scheme performs the worst with a correlation of 0.25 and RMSE of 11.36 mm. The inferior performance from the 5-imagers and GMI-only schemes can be explained by the much longer revisit time, which cannot accurately capture the emissivity temporal variation.

KEYWORDS: Precipitation; Soil moisture; Remote sensing

1. Introduction

Spaceborne passive microwave radiometers have long been recognized as key instruments for global rainfall estimates over land. Early studies in 1980s from the Scanning Multichannel Microwave Radiometer (SSMR) on board the *Nimbus-7* satellite showed that brightness temperature (TB) has a clear depression signature under thunderstorms due to the ice particles' scattering effect in the atmosphere (Spencer et al. 1983a,b). Many satellites after *Nimbus-7* carried the radiometers capable of estimating the surface rainfall rate over land via this ice scattering concept. These radiometers include Special Sensor Microwave Imager (SSMI); Special Sensor Microwave Imager/Sounder (SSMIS); Tropical Rainfall Measuring Mission Microwave Imager (TMI); Advanced Microwave Scanning Radiometer for Earth Observing System (AMSR-E) and its successor, AMSR2; Global Precipitation Measurement (GPM) Microwave Imager (GMI); Microwave Radiation Imager (MWRI); Advanced Microwave Sounding Unit-A and Unit-B (AMSU-A/B); and Advanced Technology Microwave Sounder (ATMS). Rainfall estimates from these radiometers serve as the backbone for generating the widely used global precipitation datasets, including the National Aeronautics and Space Administration's (NASA) Integrated Multisatellite Retrievals for GPM (IMERG; Huffman et al. 2015), the Climate Prediction Center's morphing technique (CMORPH; Xie et al. 2017), and the Japan Aerospace Exploration Agency's (JAXA) Global Satellite Mapping of Precipitation (GSMaP) dataset (Kubota et al. 2007).

Rainfall retrieval algorithm development has been extensively researched for these passive microwave radiometers. For example, Spencer et al. (1989) proposed the polarization-corrected temperature (PCT) to detect and retrieve rainfall over land from SSMI. Grody (1991) developed the scattering index (SI) technique to estimate the rainfall over land for SSMI, which was later improved by Ferraro et al. (1994) and Ferraro and Marks (1995). Both PCT and SI methods primarily rely on the TB observations at 85 GHz over land, which is the highest available frequency on SSMI. With the successful launch of the TRMM satellite in 1997, many retrieval algorithms for precipitation over land have also been developed for TMI (Wang et al. 2009; Gopalan et al. 2010; Petty and Li 2013b; Islam et al. 2014). In addition, retrieval algorithms have also been developed for sensors with even higher frequencies (e.g., 150 and 183 GHz), including SSMIS (You et al. 2015) and ATMS (Surussavadee and Staelin 2010; You et al. 2015). Different from these sensor-specific algorithms, generic retrieval algorithms with the capability of adapting to all these radiometers were also developed, including the Goddard

Corresponding author: Yalei You, yyou@umd.edu

DOI: 10.1175/JHM-D-20-0195.1

profiling algorithm (GPROF; Kummerow et al. 2015), the Microwave Integrated Retrieval System (MiRS; Boukabara et al. 2011), GSMaP level-2 precipitation retrieval algorithm (Aonashi et al. 2009; Shige et al. 2009), and the one-dimensional variational (1DVAR) retrieval model (Meng et al. 2017).

To more accurately estimate the surface rainfall rate, these hydrometeor-based algorithms have to mitigate the influence from the land surface, since TB reflects the integrated effect from the hydrometeors in the air and the surface emission. To this end, the entire globe is divided into 5° × 5° grid boxes in each season in the GSMaP retrieval process (Aonashi et al. 2009). Similarly, ancillary land surface type information (Aires et al. 2011) has been used by several retrieval algorithms (You et al. 2015; Kummerow et al. 2015). To largely avoid the possible surface contamination, instead of using the signatures from window channels (e.g., 85 GHz), Staelin and Chen (2000) developed a rainfall retrieval algorithm solely dependent on the microwave observations near opaque water vapor and oxygen absorption channels (183 and 52 GHz).

Brocca et al. (2014) proposed a conceptually different rainfall retrieval algorithm by using the soil moisture datasets derived from spaceborne microwave sensors. They concluded that the retrieved 5-day rainfall accumulation from the soil moisture datasets agree reasonably well with a ground gauge analysis dataset, indicated by the correlation being as large as 0.54. The ability to retrieve rainfall from the soil moisture is further demonstrated by Koster et al. (2016), which showed that satellite missions designed for soil moisture observations indeed contain valuable rainfall information. In fact, soil moisture information has also been exploited to improve the hydrometeor-based rainfall retrieval results (Crow et al. 2009; Pellarin et al. 2013).

There are key differences between these two types of rainfall algorithms, which are referred to as ''hydrometeor-based'' and ''soil-moisture-based'' retrieval algorithms for convenience. First, the microwave sensors designed for soil moisture measurement utilize lower frequencies than those suitable for hydrometeor measurement. For example, the radiometers on board the Soil Moisture Active Passive (SMAP) satellite and the Soil Moisture and Ocean Salinity (SMOS) satellite have a frequency of 1.4 GHz. The Advanced Scatterometer (ASCAT) on board the MetOp satellites operates at ~5.2 GHz. In contrast, the primary frequencies to measure the ice scattering over land from passive microwave radiometers are around 85 GHz and higher (e.g., 150 and 183 GHz). The lower frequencies used for soil moisture measurement can penetrate a thicker layer of soil and thereby provide more information about the rainfall impact on the soil, while the higher frequencies are more sensitive to the hydrometeors in the atmosphere. Second, the hydrometeor-based algorithm attempts to minimize the possible surface contamination (e.g., soil moisture, surface temperature, and vegetation). On the contrary, the soil-moisture-based algorithm attempts to limit the impact from the hydrometeors. Third, the hydrometeor-based algorithm uses the instantaneous observations at the time of the overpass, providing a snapshot of the rainfall rate at that time. In contrast, the soil-moisture-based algorithms use observations that are not contaminated by hydrometeors in the atmosphere, and therefore are more representative of accumulated rainfall over some time prior to the observation.

The objective of this study is to estimate the daily rainfall accumulation from the land surface emissivity variation due to the rainfall impact. Previous work showed that the land surface microwave emissivity tends to decrease after rainfall due to the increase of soil moisture (Jackson 1993; Ferraro et al. 2013; You et al. 2014; Yin et al. 2019). In other words, the land surface microwave emissivity variation is directly related to soil moisture change. Therefore, in essence, this work attempts to relate the soil moisture variation to the rainfall accumulation, similar to Brocca et al. (2014) and Koster et al. (2016). The key innovation is that we apply the soil-moisture-based retrieval concept to the low-frequency channels (19, 24, and 37 GHz) from 10 satellites (Table 1), instead of soil moisture-specific channels (1.4 GHz) that are only available on one or two satellites.

Previous rainfall retrieval algorithms for these 10 sensors estimated the instantaneous rainfall rate based on the ice scattering signal primarily from the high frequencies (≥85 GHz) (e.g., Ferraro et al. 2000; Ebtehaj et al. 2015; You et al. 2015; Kummerow et al. 2015; You et al. 2016). For the lower-frequency channels, the ice scattering signal is less pronounced over land due to the longer wavelength (Spencer et al. 1983a). In addition, the high and highly variable land surface emissivity often masks out the liquid raindrop emission signal at the low-frequency channels (Prigent et al. 2006; Munchak et al. 2020). For these reasons, these low-frequency channels are either not used or play a secondary role in the instantaneous rainfall retrieval process. In contrast, this study exploits the soil moisture change (instead of the hydrometeors in the air) due to the recent rainfall impact by using the nonraining observations at the low frequencies (19, 24, and 37 GHz) for daily rainfall accumulation retrieval. It is worth mentioning that the nonraining observations account for ~90% of the overall observations.

It is noted that Birman et al. (2015) used the surface emissivities at 89 GHz from multiple satellites to estimate the daily rainfall accumulation over France. As stated in the study, they use the ''effective emissivity that includes the atmospheric contribution in cases with cloudy/rainy conditions.'' By doing so, their work essentially used the hydrometeor information (instead of the soil moisture information) under raining conditions because the 89-GHz channel primarily responds to the ice-scattering signal when there are hydrometeors in the air. In other words, their work may be categorized as a hydrometeor-based retrieval algorithm under raining conditions. In contrast, this study only uses the nonraining emissivities for daily rainfall estimates at low-frequency channels including 19, 24, and 37 GHz, which is a soil-moisture-based retrieval algorithm.

The data and statistical methods used in this study are described in section 2. Section 3 presents the retrieval results from the microwave emissivity temporal variation. Finally, the conclusions are summarized in section 4.

2. Data and methodology

a. Brightness temperatures and the collocation scheme

TB observations are from 10 passive microwave radiometers, including three SSMIS on board the Defense Meteorological

TABLE 1. Channels used for rainfall retrieval from each sensor (V, vertical polarization; H, horizontal polarization). The sensors employed the cross-track scanning scheme are indicated by the superscript asterisk. Other sensors use the conical scanning scheme. For the cross-track scanning sensors, the polarization (V/H) and the mean footprint resolution are for the pixel at nadir.

Satellite name	Sensor name	Freq (GHz)	Freq (GHz)	Freq (GHz)	Freq (GHz)
GPM	GMI	18.7 (V/H, 15 km)	23.8 (V, 13 km)	36.6 (V/H, 12 km)	89.0 (V/H, 7 km)
GCOM-W1	AMSR2	18.7 (V/H, 22 km)	23.8 (V/H, 26 km)	36.5 (V/H, 12 km)	89.0 (V/H, 5 km)
F16	SSMIS	19.4 (V/H, 59 km)	21.3 (V, 59 km)	37.0 (V/H, 36 km)	85.5 (V/H, 14 km)
F17	SSMIS	19.4 (V/H, 59 km)	21.3 (V, 59 km)	37.0 (V/H, 36 km)	85.5 (V/H, 14 km)
F18	SSMIS	19.4 (V/H, 59 km)	21.3 (V, 59 km)	37.0 (V/H, 36 km)	85.5 (V/H, 14 km)
SNPP	ATMS*		23.8 (V, 75 km)	31.4 (V, 75 km)	88.2 (V, 32 km)
NOAA-18	AMSU-A*		23.8 (V, 48 km)	31.4 (V, 48 km)	89.0 (V, 16 km)
NOAA-19	AMSU-A*		23.8 (V, 48 km)	31.4 (V, 48 km)	89.0 (V, 16 km)
MetOp-A	AMSU-A*		23.8 (V, 48 km)	31.4 (V, 48 km)	89.0 (V, 16 km)
MetOp-B	AMSU-A*		23.8 (V, 48 km)	31.4 (V, 48 km)	89.0 (V, 16 km)

Satellite Program (DMSP) *F16*, *F17*, and *F18* satellites; AMSR2 on board the *Global Change Observation Mission–Water* (*GCOM-W1*) satellite; GMI on board the GPM *Core Observatory* satellite; four AMSU-A on board *NOAA-18*, *NOAA-19*, *MetOp-A*, and *MetOp-B* satellites; and ATMS on board the *Suomi National Polar-Orbiting Partnership* (*SNPP*) satellite. The channels used in study and their mean footprint resolution are listed in Table 1. These channels often have different footprint resolutions. It is necessary to bring these channels to a common resolution.

This study takes the 19-GHz footprint of SSMIS as the "nominal" resolution primarily because it has the coarsest resolution among all the imagers' channels (GMI, SSMIS, and AMSR2, Table 1). It is much easier to downgrade the finer resolutions to this coarser resolution than vice versa. Additionally, we derive the emissivity temporal variation later in each 0.5° grid box, and this approximately corresponds to the 19-GHz resolution of SSMIS (59 km) in the tropical region. The much finer spatial resolution footprints (e.g., 5 km) are averaged (downgraded) to this coarser resolution by selecting the closest n pixels to the nominal pixel footprint. The variable n is calculated in a way that the area of the finer-resolution footprints is approximately the same as that from the nominal resolution (59 km). The footprints with coarser resolution (e.g., 75 km) and resolution close to 59 km (i.e., 48 km) remain unchanged.

Specifically, for SSMIS we average 18 ($59 \times 59/14/14 \approx 18$) pixels of 85.5 GHz and 3 pixels of 37.0 GHz to match this nominal resolution. The resolution at 21.3 GHz is kept the same. For GMI, we average 16 ($59 \times 59/15/15 \approx 16$) pixels of 18.7 GHz, 21 pixels of 23.8 GHz, 25 pixels of 36.6 GHz, and 71 pixels of 89 GHz to approximately match the 59-km resolution. For AMSR2, we average 8 pixels of 18.7 GHz, 5 pixels of 23.8 GHz, 25 pixels of 36.5 GHz, and 140 pixels of 89.0 GHz to match the nominal resolution. For both ATMS and AMSU-A, the resolution at 23.8 and 31.4 GHz remains unchanged. We

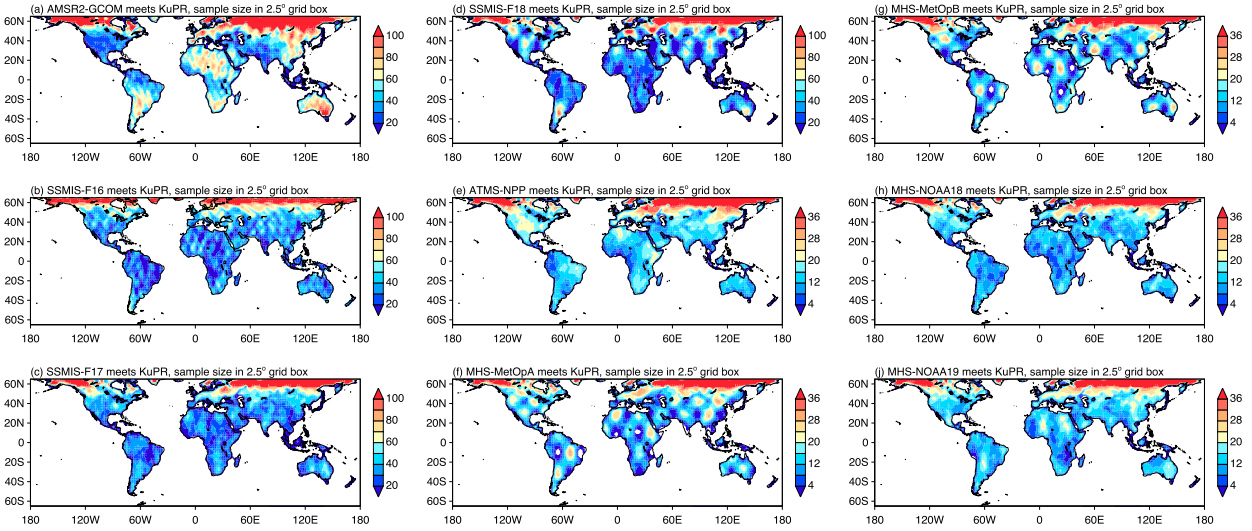

FIG. 1. Coincident observation number in each 2.5° grid box between GMI and nine other sensors, including AMSR2, SSMIS-*F16*, SSMIS-*F17*, SSMIS-*F18*, ATMS-*SNPP*, AMUSA-*MetOp-A*, AMSUA-*MetOp-B*, AMSUA-*NOAA-18*, and AMSUA-*NOAA-19*. The number is scaled by 100 in each plot. All data are from March 2014 (launch of the GPM satellite) to December 2018.

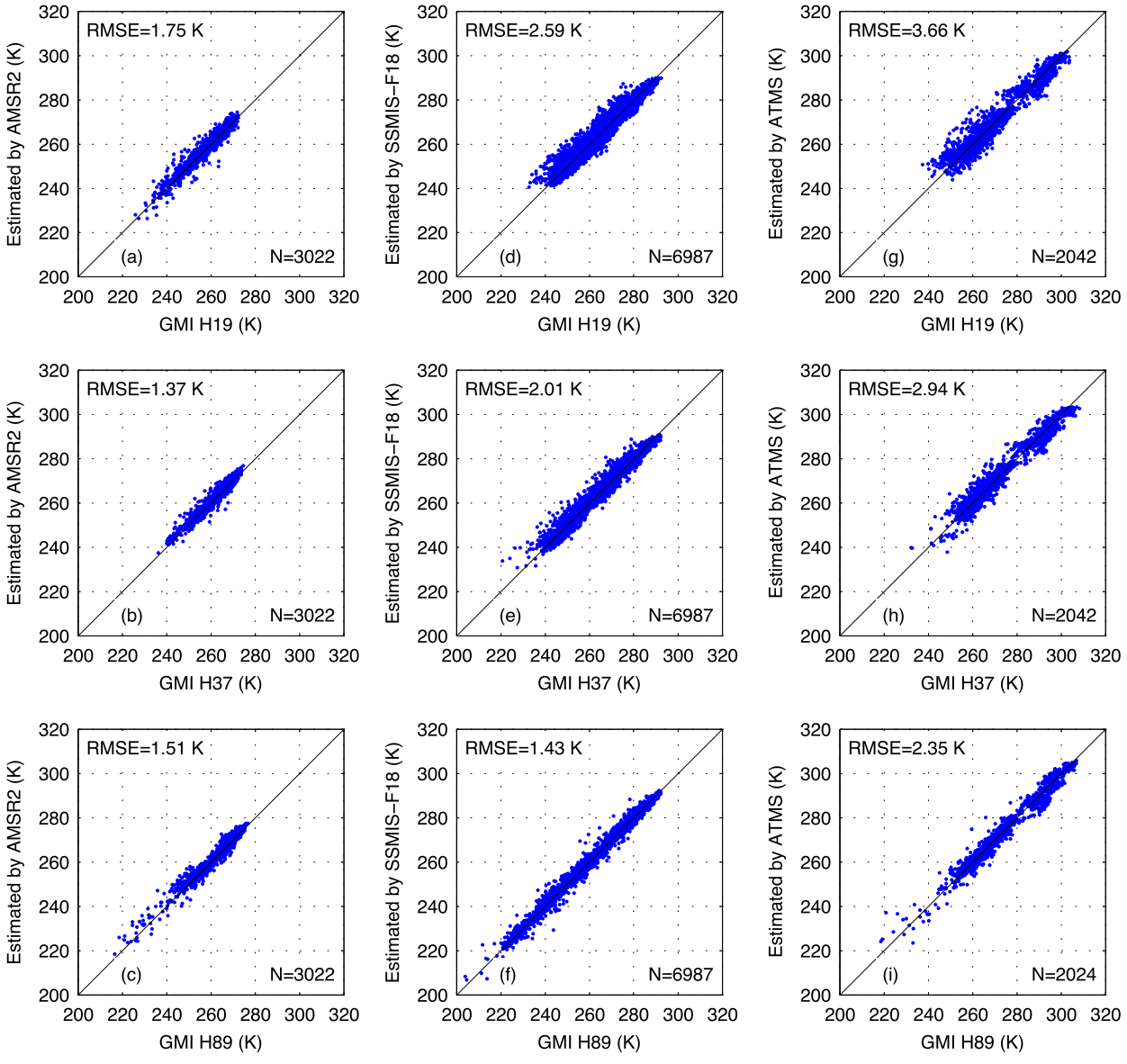

FIG. 2. Scatterplots between GMI TBs and estimated TBs from AMSR2 at (a) H19, (b) H37, and (c) H89, using the simultaneous conical overpass pairs between GMI and AMSR2 over the grid box of 32°N, 103°W from March 2014 (launch of the GPM satellite) to December 2018. (d)–(f) As in (a)–(c), but between GMI and SSMIS-*F18*. (g)–(i) As in (a)–(c), but between GMI and ATMS-*SNPP*.

average 4 pixels of 88.2 GHz from ATMS and 14 pixels of 89.0 GHz from AMSU-A to match the nominal resolution of 59 km.

b. *Convert TB from other nine sensors to TB at the GMI frequencies*

As shown in Table 1, the frequencies among these 10 radiometers are not identical. The slight frequency difference results in different TBs for the same surface background and hydrometeor profile (Yang et al. 2014). In the following discussion, we demonstrate a method to convert TBs from other nine sensors to GMI frequencies. For convenience, we do not distinguish the slight frequency differences among these sensors from now on unless otherwise specified. These channels are referred to as V19, H19, V24, V37, H37, V89, and H89.

This study is to estimate rainfall accumulation by emissivity temporal variation derived from these TB observations. To this end, it is necessary to convert all TBs at similar frequencies to the same frequency. The conversion process has been detailed in You et al. (2017, 2018). Here, only a brief summary is provided.

The following discussion takes the GMI and SSMIS (*F18*) as an example to discuss the conversion process, which can be summarized into four steps:

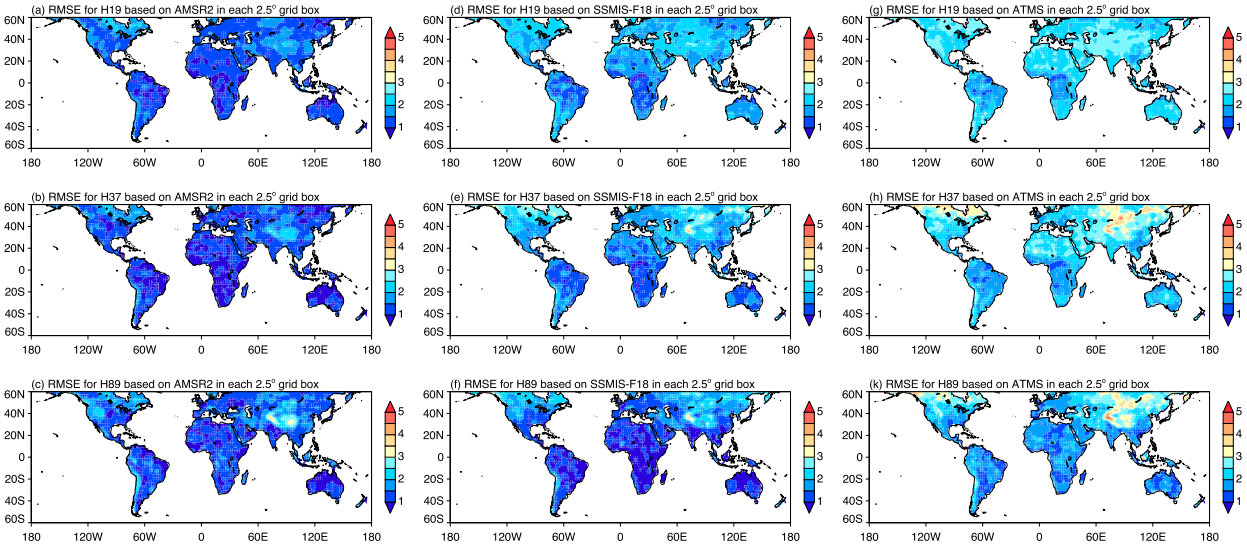

FIG. 3. The RMSE in each 2.5° grid box between GMI and AMSR2 at (a) H19, (b) H37, and (c) H89. (d)–(f) As in (a)–(c), but between GMI and SSMIS-*F18*. (g)–(i) As in (a)–(c), but between GMI and ATMS-*SNPP*. All data are from March 2014 (launch of the GPM satellite) to December 2018.

1) Find the simultaneous conical overpass (SCO) pairs between GMI and SSMIS (Yang et al. 2011; You et al. 2017, 2018). The SCO pairs are pixels from these two satellites, which are at most 5 km apart and 5 min away.
2) Decompose the GMI TBs from these SCO pairs into principal components (PCs).
3) Use the SSMIS TBs in these SCO pairs to estimate the first several PCs by a linear regression model. This study selects the first four PCs, which accounts for over 90% of the total variance.
4) Apply the coefficients derived from the SCO pairs to the whole SSMIS data. By doing so, we obtain the estimated PCs from SSMIS. These PCs are converted back to TBs at the GMI frequencies.

The same procedure is applied to AMSR2, SSMIS (*F16* and *F17*), ATMS, and AMSU-A. The V37-GHz channel from *F17* is not used since the data from April 2016 are not processed by the calibration team due to the large noise. The missing V37 channel on *F17* SSMIS shows little influence on the TB conversion. On the other hand, both ATMS and AMSU-A only have the vertically polarized channels, and both radiometers do not have channels around 19 GHz. Later analyses will show that the root-mean-square error (RMSE) from the TB conversion based on ATMS and AMSU-A is noticeably larger than those from AMSR2 and SSMIS. However, section 3 clearly demonstrates the improved rainfall retrieval performance by including these five sounders due to the increased sample size.

In contrast to our previous studies (You et al. 2017, 2018), this study applies the TB conversion procedure at each 2.5° grid box. By doing so, we show later that RMSE from this conversion is less than 3 K over almost all the areas from 60°S to 60°N. After this TB conversion process, GMI and other nine sensors all have channels of V19, H19, V24, V37, H37, V89, and H89.

c. *Rainfall datasets*

The half-hour IMERG Final run (version 06A) product at 0.1° is used to investigate the rainfall impact duration period. These IMERG data are downgraded to the 0.5° spatial resolution by the simple arithmetic average, which is also taken as the surface "reference" rainfall dataset for retrieval. In addition, we use the KuPR rainfall observations along with the GMI TB observations to train a rain/no-rain screening method, which is applied to all TB observations to filter out the raining pixels.

Data in this study are all from March 2014 (launch of the GPM satellite) to December 2018 over the 60°S–60°N land areas.

d. *Ancillary parameters*

To derive the land surface emissivity, we use hourly surface temperature and 3-hourly temperature and humidity profiles at the 0.5° × 0.625° resolution from Modern-Era Retrospective Analysis for Research and Applications, version 2 (MERRA-2) (Gelaro et al. 2017). We also use the NOAA National Environmental Satellite, Data, and Information Service's (NESDIS) daily Global 4 km Multisensor Automated Snow/Ice Map (GMASI) to filter out pixels associated with the snow/ice on the ground (Romanov 2017).

e. *Rainfall detection by LDA*

The objective of this study is to use the emissivity under nonraining conditions to retrieve daily rainfall accumulation. To this end, we use the linear discriminant analysis (LDA) approach (Turk et al. 2014; You et al. 2015) to filter out the raining pixels. This method is first developed based on GMI and KuPR observations, then applied to converted TBs from other nine sensors.

Suppose there exist two training databases from KuPR (i.e., raining versus nonraining databases), which contain multivariables **x** (i.e., V19, . . . , H89) in each database. According to

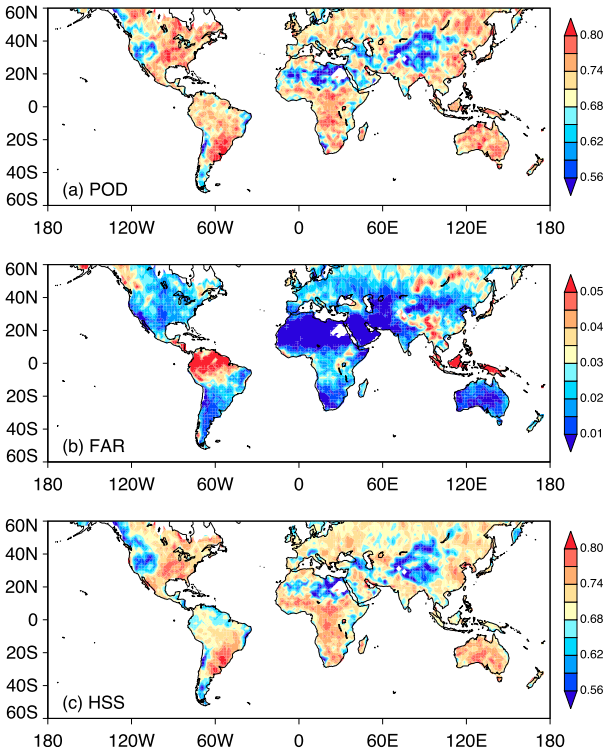

FIG. 4. (a) The POD at each 2.5° grid box, derived from GMI and KuPR observations from March 2014 (launch of the GPM satellite) to December 2018 at the nominal resolution of 59 km. (b) As in (a) but for FAR. (c) As in (a), but for HSS.

Wilks (2011) the linear discriminant function to distinguish these two groups is

$$\delta_1 = \mathbf{a}^{\mathrm{T}} \times \mathbf{x}, \tag{1}$$

where the superscript T stands for the transpose. The term **a** is the discriminant vector, calculated in the following way:

$$\mathbf{a} = \mathbf{S}_{\mathrm{pool}}^{-1}(\bar{\mathbf{x}}_1 - \bar{\mathbf{x}}_2),$$

$$\mathbf{S}_{\mathrm{pool}} = \frac{n_1 - 1}{n_1 + n_2 - 2}\mathbf{S}_1 + \frac{n_2 - 1}{n_1 + n_2 - 2}\mathbf{S}_2; \tag{2}$$

$\bar{\mathbf{x}}_i$ and $\mathbf{S}_i$ $(i = 1, 2)$ represent the mean vector and covariance of each group, respectively. The matrix $\mathbf{S}_{\mathrm{pool}}$ is the weighted average of the two sample covariance matrices from these two datasets, and n_1 and n_2 are the samples size in these two groups, respectively.

To assess the rainfall detection performance, four numbers in a 2×2 contingency table (hit, miss, false alarm, and correct negative) are computed (Wilks 2011). A hit (referred to as a) is defined as both the reference (KuPR) and the LDA method detecting rainfall. A false alarm (b) is when the LDA method detects rainfall while the reference does not, while a miss (c) is when the reference detects rainfall but the LDA method does not. A correct negative (d) is when both the reference and the LDA method detect no rainfall.

This study further computes the accuracy metrics derived from these four numbers, including probability of detection (POD), false alarm rate (FAR), and Heidke skill score (HSS). These metrics are calculated as follows:

$$\mathrm{POD} = \frac{a}{a + c},$$

$$\mathrm{FAR} = \frac{b}{b + d},$$

$$\mathrm{HSS} = \frac{2(ad - bc)}{(a + c)(c + d) + (a + b)(b + d)}. \tag{3}$$

The POD (FAR) values vary from 0 to 1 with a larger POD (smaller FAR) indicating better detection performance. We use the HSS value to judge the overall detection performance with a larger HSS value indicating a better overall performance.

f. *Emissivity computation*

We compute the emissivity values for each pixel at different channels based on Munchak et al. (2020), which is briefly summarized here. The emissivity vector is calculated from the converted brightness temperatures (i.e., other satellites' observations are converted to the GMI channel set). This allows us to use the same atmospheric absorption and incidence angle assumptions that are used for GMI in Munchak et al. (2020). The emissivity and atmospheric temperature and water vapor profile are retrieved using an optimal estimation inversion procedure. For the set of channels used in this study, however, there is little independent information about the atmospheric profile, and the retrieved emissivities are essentially those that reproduce the converted brightness temperatures, given the space–time interpolated MERRA2 skin temperature and atmospheric profile.

g. *Emissivity temporal variation definition*

To derive emissivity temporal variation, it is necessary to determine when the observations from different satellites are considered as observations for the same location. This study first divides the globe into a 0.5° grid box. We define any observation in the same 0.5° latitude–longitude grid box as observations at the same location. We choose the 0.5° grid box because the nominal resolution (59 km) is approximately 0.5° in the tropical region. Choosing a different grid size (e.g., 0.25° or 1°) does not affect the major conclusions of this work.

The emissivity e temporal variation Δe is defined as

$$\Delta e = e_{t_0} - e_{t_{-1}}, \tag{4}$$

$$\Delta t = t_0 - t_{-1}, \tag{5}$$

where e_{t_0} is the current daily mean emissivity when rainfall occurs, and $e_{t_{-1}}$ is the preceding daily mean emissivity at the same location without rainfall. The daily emissivity is computed as the arithmetic mean from the selected satellites (e.g., all 10 satellites or imagers only, see section 3e for details). A day is judged as raining day when there is at least one raining observation on that day. No raining pixels are included in the daily mean emissivity average process. The time difference between these two days is Δt. From now on, the Δe at V19, H19, . . . , V89 will be referred to as Δe_{v19}, Δe_{h19}, . . . , Δe_{v89} for convenience.

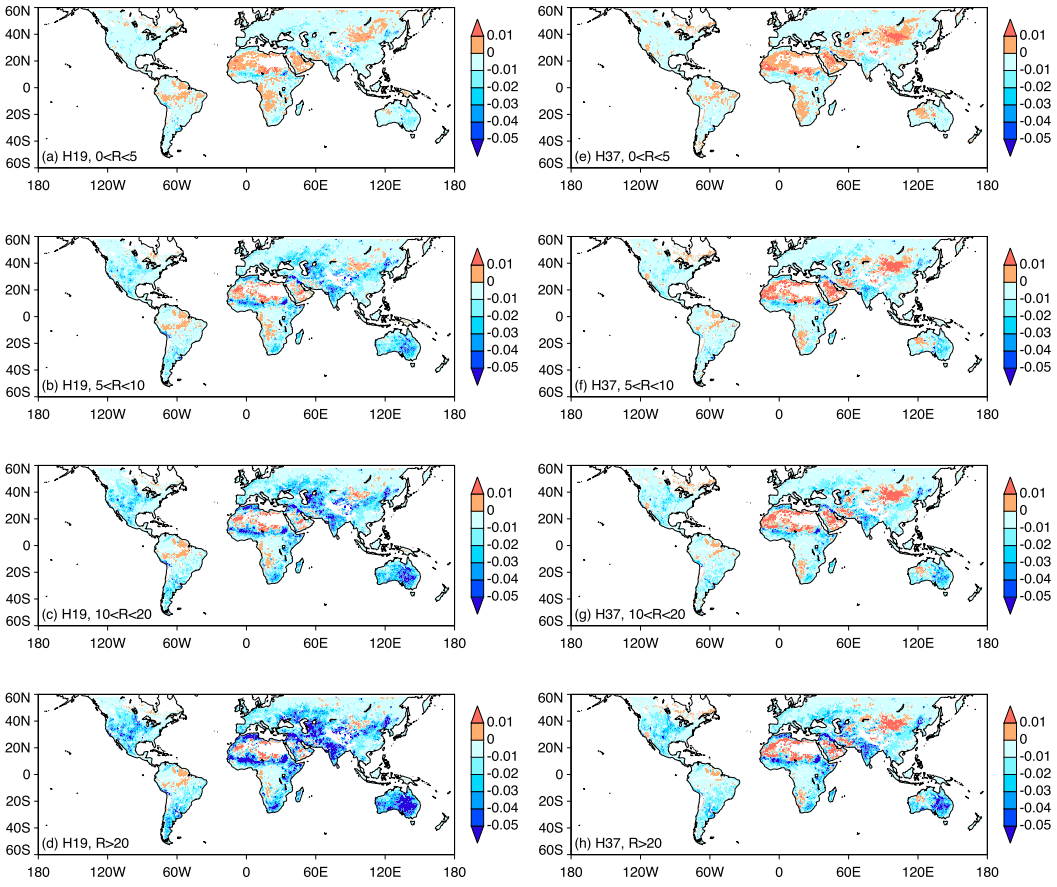

FIG. 5. (a)–(d) Emissivity at H19, wet (rainfall occurs on previous one day) minus dry (no rainfall on previous one day) conditions. The rainfall accumulation (R) on previous 1 day is separated into four categories ($0 < R < 5, 5 \le R < 10, 10 \le R < 20$, and $R \ge 20$), which is computed from the half-hour IMERG final run (version 06A) product. (e)–(h) As in (a)–(d), but for H37.

h. Bayesian retrieval method

To retrieve the daily rainfall accumulation from Δe, we adopt the Bayesian retrieval technique as implemented by You et al. (2016). It is worth mentioning that the Bayesian retrieval concept is widely used in the precipitation/cloud retrieval community (e.g., Evans et al. 1995; Kummerow et al. 1996; Chiu and Petty 2006; Noh et al. 2006; Kim et al. 2008; Sano et al. 2013; Petty and Li 2013a; You et al. 2015, 2016).

Mathematically, the retrieval method can be stated as follows:

$$f(x|\mathbf{y}) = \frac{f(\mathbf{y}|x) \times f(x)}{f(\mathbf{y})} = \frac{f(\mathbf{y}|x) \times f(x)}{\int f(\mathbf{y}|x) \times f(x)\, dx}, \tag{6}$$

where x and $\mathbf{y}$ represent the daily rainfall amount and the emissivity temporal variation vector [Δe_{v19}, Δe_{h19}, Δe_{v24}, Δe_{v37}, Δe_{h37}], respectively. Later analyses will show that emissivity at 89 GHz has very weak response to the previous rainfall, compared with the low frequencies. Therefore, in the rainfall retrieval process, we only include the emissivity at 19, 24, and 37 GHz and emissivity at 89 GHz is not used. The term $f(x|\mathbf{y})$ is the posterior probability density function (PDF) of x given the $\mathbf{y}$, $f(x)$ is the prior PDF of x and $f(\mathbf{y}|x)$ is the likelihood function of $\mathbf{y}$ given the precipitation rate x.

The expected value of x is taken as the final estimation for the daily rainfall amount, which is computed in the following way:

$$E(x|\mathbf{y}) = \frac{\int x \times f(\mathbf{y}|x) \times f(x)\, dx}{\int f(\mathbf{y}|x) \times f(x)\, dx},$$

$$E(x|\mathbf{y}) = \frac{\int x \times f(\mathbf{y}|x) \times f(x)\, dx}{\int f(\mathbf{y}|x) \times f(x)\, dx} = \frac{E[x \times f(\mathbf{y}|x)]}{E[f(\mathbf{y}|x)]}, \tag{7}$$

where E stands for the expectation.

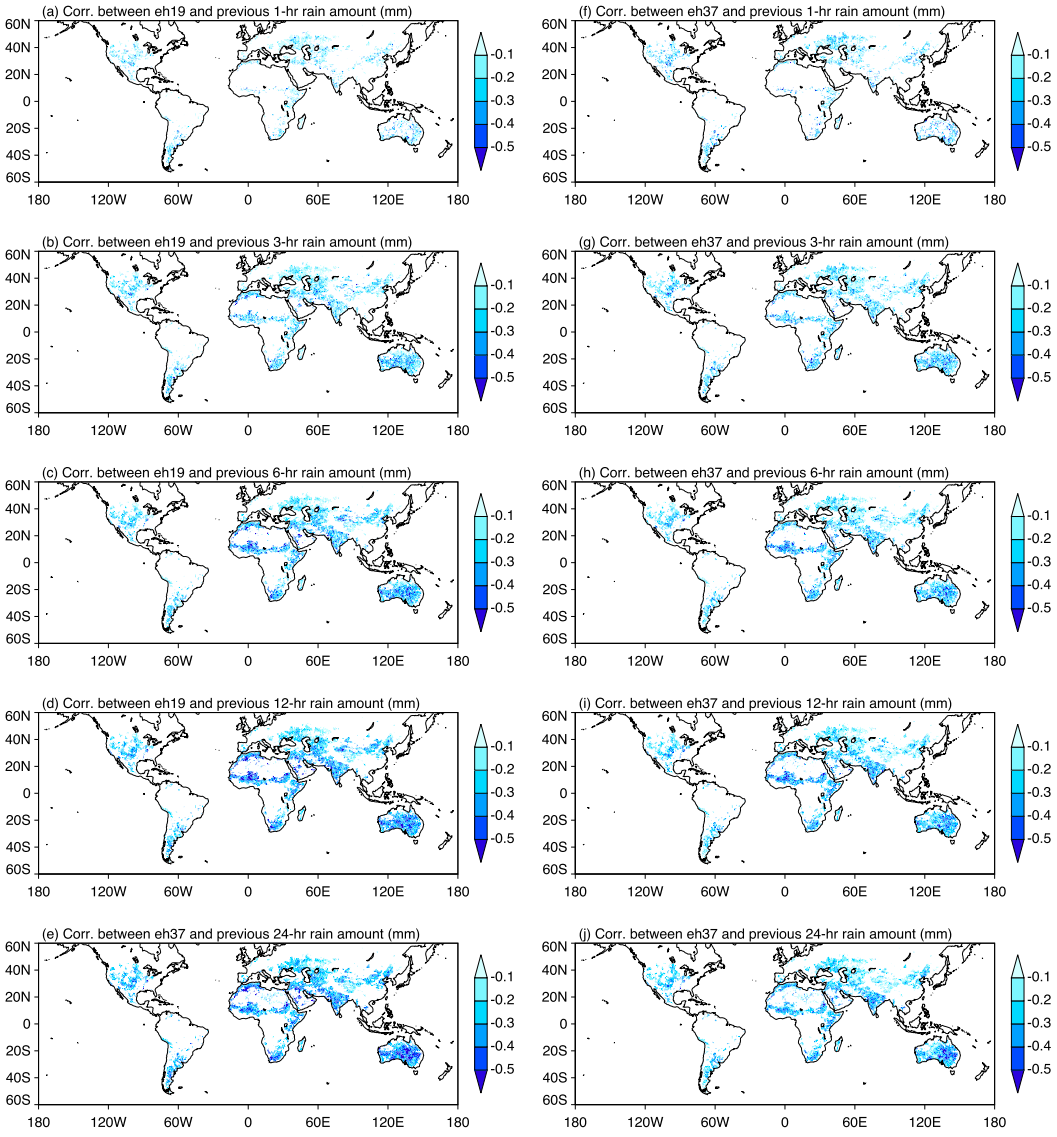

FIG. 6. (a)–(e) Correlation between emissivity at H19 (e_{h19}) and the previous n-hour rainfall accumulation, where n stands for 1, 3, 6, 12, and 24, respectively. (f)–(j)As in (a)–(e), but for emissivity at H37 (e_{h37}). Rainfall accumulation is computed from the half-hour IMERG final run (version 06A) product.

3. Results

This section first shows the TB conversion and the rain/no-rain detection statistics. Then, we explain how to determine the rain-sensitive region based on the emissivity depression corresponding to the different daily rainfall amount. We also explain why we would like to retrieve the daily rainfall amount, instead of multiple-day rainfall accumulation. Finally, we present the retrieval results from four different satellite constellation experiments and demonstrate why satellites with varying equator crossing times (ECTs) are necessary for the best retrieval performance.

a. Brightness temperature conversion statistics

TBs from other satellites are converted to GMI frequencies for the temporal variation computation. Figure 1 shows the sample size of the SCO pairs in each 2.5° grid box between GMI and other nine sensors over land. It is found that the sample size in the vast majority of boxes (>99%) for all satellites is greater than 200, which is sufficient to ensure the conversion coefficients are stable. In case there are not enough SCO pairs (<200) in some grid boxes, especially from *MetOp-A* (Fig. 1f) and *MetOp-B* (Fig. 1g), we aggregate the SCO pairs in the nearest several grid boxes until the sample size is greater than 200. This number (200) is selected through trial and error by considering the trade-off between the regression coefficients' stability and regional features.

A case study is selected to demonstrate the TB conversion performance. Figure 2 shows a conversion case study at H19, H37, and H89 at the grid box of 32.5°N, 103°W between GMI and AMSR2 (Figs. 2a–c), between GMI and SSMIS-*F18*

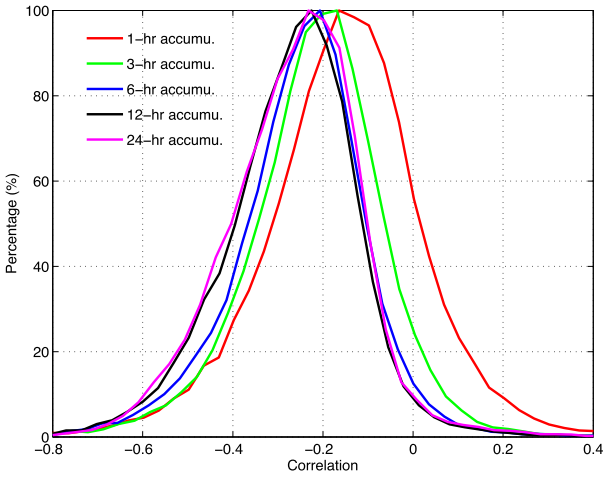

FIG. 7. Histogram of correlation coefficients between emissivity at H19 (e_{h19}) and the previous n-hour rainfall accumulation, where n stands for 1, 3, 6, 12, and 24. For comparison, all histograms are vertically scaled to unity by their maximum histogram frequency counts. Rainfall accumulation is computed from the half-hour IMERG Final run (version 06A) product.

(Figs. 2d–f), and between GMI and ATMS (Figs. 2g,h). The plots from SSMIS-*F16* and SSMIS-*F17* are similar to those from SSMIS-*F18*. The plots from four AMSU-A sensors are similar to those from ATMS. It is noticed that the estimated GMI TBs from these three satellites are very close to GMI observations. In fact, the correlation from all these channels are over 0.95, and the bias is close to 0, which indicates that the conversion is working correctly. The RMSE (shown on the figure) is less than 3 K, except the estimated H19 from ATMS. As mentioned earlier, ATMS does not have frequency around 19 GHz. Also, only the vertically polarized channels are available from ATMS (Table 1). These two ATMS features are responsible for the larger RMSE from ATMS. Similarly, RMSE from H19 estimated from AMSU-A is also noticeably larger than those from AMSR2 and SSMIS. Further, RMSE at H19 and H37 from AMSR2 is smaller than those from SSMIS, which is likely due to the finer footprint resolution from AMSR2, and the almost identical frequencies between GMI and AMSR2. At 89 GHz, RMSE from AMSR2 (Fig. 2c) and SSMIS-*F18* (Fig. 2f) is comparable, likely due to the large impact of the hydrometeors in the atmosphere.

The global RMSE distribution further confirms the effectiveness of the TB conversion process, which is shown in Fig. 3 for AMSR2, SSMIS-*F18*, and ATMS. Our analysis shows that over 95% of the grid has a RMSE less than 3 K, which corresponds to ~0.01 emissivity error. Consistent with the case study, RMSE from ATMS is the largest in almost all regions. RMSE at H19 and H37 GHz from AMSR2 is noticeably smaller than those from SSMIS (cf. Fig. 3a and Fig. 3d, cf. Fig.3b and Fig. 3e). For H89 channel, RMSE from SSMIS and AMSR2 are of comparable magnitude. Analysis has also been conducted for all the vertically polarized channels (V19, V24, V37, and V89), yielding very similar results to those from the horizontally polarized channels.

b. *Rainfall detection statistics*

Similar to the TB conversion process, we refine our previously developed LDA rainfall detection method by applying it to each 2.5° grid box. To ensure the stability of the detection statistics, the number of raining pixels in each 2.5° grid box is required to be at least 500. When there are less than 500 raining pixels, we aggregate the observations in the nearest several 2.5° grid boxes until the sample size is greater than or equal to 500. At each grid box, a discriminant threshold value is selected to maximize the HSS.

Our detection method demonstrates reliable rainfall detection performance. Figure 4 shows that the POD and HSS are over 0.7 over the majority of the region, and the FAR is less than 0.05 over most of the region. These detection statistics are similar to those from the official NASA and JAXA precipitation detection algorithms (You et al. 2020).

We would like to emphasize that in the daily rainfall estimation process, we first filter out the raining pixels judged by the LDA detection method. Therefore, the signal we use is essentially the soil emission variation due to the rainfall impact, not the hydrometeors' effect in the air.

c. *Rainfall sensitive regions*

Previous studies (Brocca et al. 2014; McColl et al. 2017) showed that rainfall has little impact on the land surface soil moisture derived from microwave radiometer observations at 1.5 GHz over densely vegetated regions (e.g., the Amazon, Central Africa, and the eastern United States). This study primarily exploits the soil moisture change due to the recent rainfall impact at the low-frequency channels. Therefore, we would like first to select rainfall sensitive regions, by assessing the surface emissivity response to rainfall over different regions. This analysis is based on the emissivity derived from GMI only to reduce the computational time, instead of from all 10 satellites.

It is known that land surface emissivity tends to decrease due to the soil moisture increase. Figure 5 shows the emissivity depression at H19 and H37 corresponding to different previous 1-day rainfall accumulation. Specifically, we obtain the previous 1-day rainfall amount corresponding to each pixel from the half-hour IMERG Final run product. Then, we compute the emissivity differences between wet (rainfall occurs in the previous one day) and dry (no rainfall in the previous one day) conditions at the 0.5° resolution. For the wet condition, the previous 1-day rainfall accumulation (indicated by R on the Fig. 5) is further grouped into four categories, including $0 < R < 5$, $5 < R < 10$, $10 < R < 20$, and $R > 20$ mm.

As illustrated in Fig. 5, emissivity decreases over most of the land areas after rainfall events in the previous day, and the emissivity depression increases as the rainfall amount becomes larger. The emissivity drop is particularly evident with rainfall accumulation greater than 20 mm over the Sahel, southern Africa, the Middle East, the Indian subcontinent, northwest China, Australia, and the western United States (Figs. 5d,h). As expected, the emissivity depression magnitude is smaller at H37 than at H19 since 19 GHz is more sensitive to the surface properties (e.g., soil moisture). The emissivity depression at

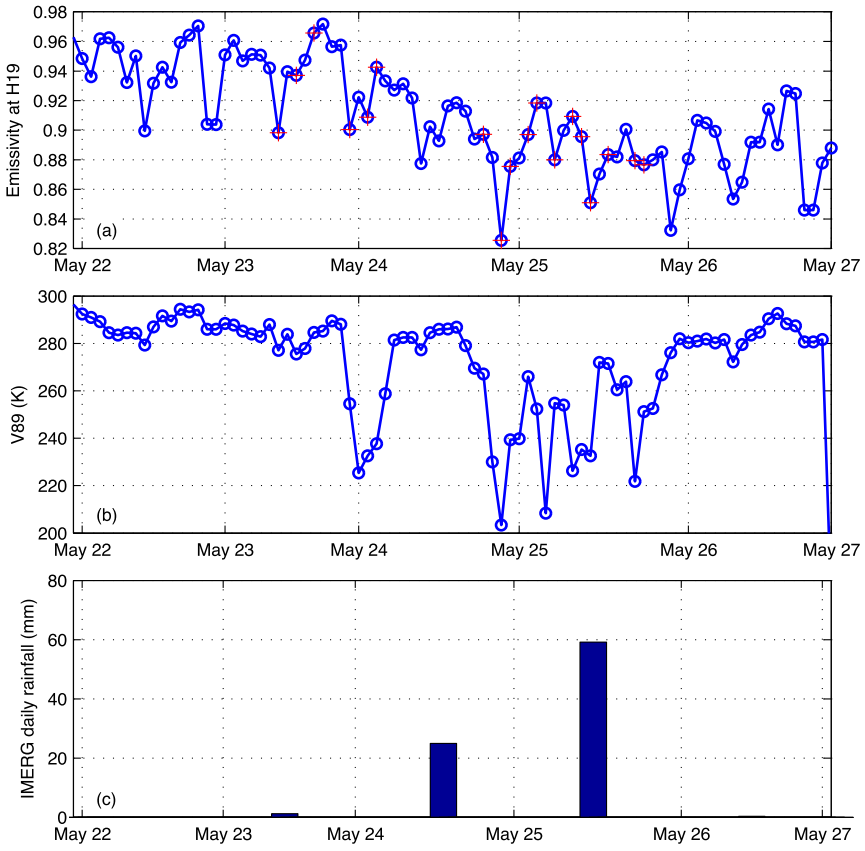

FIG. 8. (a) Time series of emissivity at H19 (e_{h19}) from 21 to 26 May 2014 at the grid box 32°N, 100°W. The blue circle indicates the satellite observations, and the red cross indicates the raining pixels judged by the LDA method, which are discarded in the retrieval process. (b) As in (a), but for V89. (c) Daily IMERG rainfall accumulation from 21 to 26 May 2014 at the grid box 32°N, 100°W.

H89 (not shown) is even smaller than H37. Similar analysis has also been performed for the vertical polarized channels, from which the rainfall response is weaker than their horizontally polarized counterparts. These features (e.g., lower frequency with larger emissivity drop due to the rainfall impact) are well known from previous studies (Jackson 1993; Ferraro et al. 2013; You et al. 2014; Munchak et al. 2020). Based on these analyses, we only use the emissivity values at V19, H19, V24, V37, and H37 for the daily rainfall retrieval and no emissivity values from 89 GHz are included in the retrieval process.

This study attempts to exploit the emissivity depression signature due to the recent rainfall impact. For this purpose, we define regions with emissivity drop of at least 0.02 with previous 1-day rainfall accumulation greater than 20 mm as "rainfall-sensitive regions" and retrieval is only performed over these regions. We select this threshold value (0.02) because the combined uncertainty from the TB conversion and the emissivity retrieval process is approximately 0.02. This threshold value also balances the retrieval performance and the availability of regions where our method is applicable. Choosing a smaller value (e.g., including almost all regions by using 0 as the threshold value) leads to a worse retrieval performance because rainfall events have little impact on the emissivity over the densely vegetated regions (e.g., Amazon and Central Africa). On the other hand, choosing a larger value (e.g., 0.04) limits where our retrieval method is applicable, without an appreciable increase in retrieval performance.

d. *Correlation between emissivity and rainfall accumulation at different time scales*

It is desirable to understand how long the rainfall impact can last. To this end, we compute the correlation between emissivity under rain-free conditions and previous *n*-hour rainfall accumulation at the 0.5° resolution over the rainfall-sensitive regions. Similar to the rainfall-sensitive analysis, this analysis also only uses the emissivity derived from GMI to reduce the computational time.

We first attach the previous rainfall accumulations of 1, 3, 6, 12, and 24 h to each emissivity pixel. Then, we compute the correlation between emissivity and these rainfall accumulations at each 0.5° grid box. The purpose is to check when the correlation peaks. Figure 6 shows that the correlation magnitude between emissivity and rainfall accumulation increases quickly from 1 h (Fig. 6a) to 12 h (Fig. 6d) for H19, which is

especially evident over Australia. While for the correlation from 12 h (Fig. 6d) to 24 h (Fig. 6e), such an increase is marginal. The H37 channel exhibits similar correlation temporal variations (Figs. 6f–j).

To more clearly show this correlation variation, we plot the histogram of the correlation between emissivity and previous n-hour rainfall accumulation (n varies from 1 to 24 h). The curves corresponding to 12 h (black) and 24 h (purple) are heavily overlapped (Fig. 7), demonstrating that the correlations between emissivity and 12-h rainfall accumulation is very similar to the correlation between emissivity and 24-h rainfall accumulation. This implies that previous rainfall being 13–24 h away from that pixel has little impact to the emissivity value of that pixel. In other words, rainfall impact at H19 and H37 often persists about 12 h. Therefore, this behavior supports our goal to estimate the daily rainfall accumulation. Of course, the rainfall impact can propagate into the next day, depending on at which hour the rainfall occurs. While 2- or 3-day accumulations might be more accurate, most applications prefer daily accumulations.

e. *Rainfall retrieval result*

This section begins with a case study to explain in detail how the retrieval algorithm is implemented. Then we test four retrieval experiments to show why using 10 satellites produces the most accurate retrieval result.

Figure 8a shows the time series of emissivity at H19 over a selected grid box (32°–32.5°N, 99.5°–100°W) in the central Texas region. The LDA detection approach indicates that rainfall occurs on 23, 24, and 25 May 2014 (shown as red crosses). On 24 and 25 May 2014, these rainfall occurrences correspond very well with the ''cold'' TB at V89, shown in Fig. 8b. On 23 May 2014, the TB depression at V89 is not as obvious as that on 24 and 25 May 2014. However, IMERG rainfall product indeed shows the daily rainfall amount at 1.2 mm on 23 May 2014.

The daily rainfall retrieval algorithm takes the following steps: 1) filter out the raining pixels (indicated by the red crosses) from 23 to 25 May 2014 because the computed emissivities for these pixels are affected by the hydrometeors in the atmosphere; 2) compute the daily mean emissivity using the nonraining values; 3) compute the daily mean emissivity on the preceding nonraining day (i.e., 22 May 2014, background emissivity); 4) obtain the emissivity difference between raining day (23–25 May 2014) and background emissivity (22 May 2014). For demonstration purposes, Fig. 8a only shows the emissivity temporal variation at H19. In the retrieval process, we use the emissivity variation at 19, 24, and 37 GHz (i.e., Δe_{h19}, Δe_{v19}, Δe_{h24}, Δe_{v37}, Δe_{h37}). This Δe computation procedure is applied at each 0.5° grid box over the rainfall-sensitive regions.

Next, we design four experiments to demonstrate the advantages of using multiple satellites. In each experiment, we randomly select 80% data at each grid box as the training dataset, while the retrieval is performed on the other 20% data. In the first experiment, Δe at each channel is calculated by GMI observations only. The second experiment computes Δe using all five imagers (four sun-synchronous satellites shown in blue color in Fig. 9), including GMI, AMSR2, and three SSMISs. Clearly, the ECTs from *F17* and *F18* are, on average, only about 10 min apart, indicating that they observe the same location at nearly the same time of day. In the third experiments, we select six sensors, including GMI and five other radiometers on board the sun-synchronous satellites (i.e., AMSR2 on board *GCOM-W1*, AMSU-A on board *NOAA-19*, SSMIS on board *F16* and *F17*, and AMSU-A on board *MetOp-A*). The selection of these five sun-synchronous sensors is based on the fact that ECTs from them are very different, as shown in Fig. 9. By doing so, the emissivity temporal variation can be better captured. The fourth experiments use observations from all 10 sensors to compute Δe. For convenience, these four experiments are referred as ''GMI only,'' ''5 imagers,'' ''6 satellites,'' and ''all 10 satellites.''

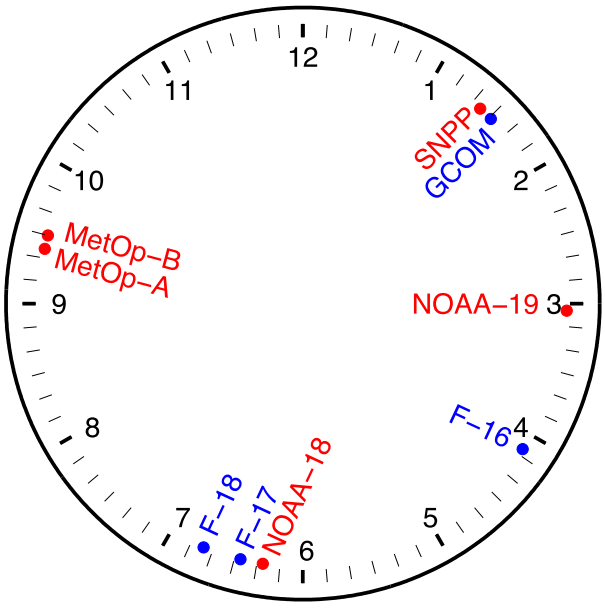

FIG. 9. Equator crossing time (local time in the morning) for nine sun-synchronous satellites. Satellites with imagers on board are in blue (i.e., AMSR2 on board *GCOM-W1*, SSMIS on board *F16*, *F17*, and *F18*), and satellites with sounders on board are in red (i.e., ATMS on board *SNPP*, AMSU-A on board *NOAA-18*, *NOAA-19*, *MetOp-A*, *MetOp-B*). The GPM satellite has a precessing orbit, which means that it overpasses a certain location at varying times throughout the day.

When only the GMI is used to compute Δe, the retrieval performance is rather poor, as indicated by the correlation being 0.25 and RMSE being 11.36 mm (Fig. 10a). It is immediately clear that the 5-imagers scheme produces much improved retrieval results. Specifically, the correlation increases to 0.49 and RMSE decreases to 7.28 mm (Fig. 10b). Further analysis reveals several reasons responsible for this large retrieval improvement, which are all related to the observation sample size. First, the time difference [i.e., Δt in Eq. (2), the time difference between the raining day and the nonraining day] is shorter when using five imagers than only using GMI, as shown in Fig. 11. The time difference is 1 day for over 85% cases when using five imagers, which means that one can find a

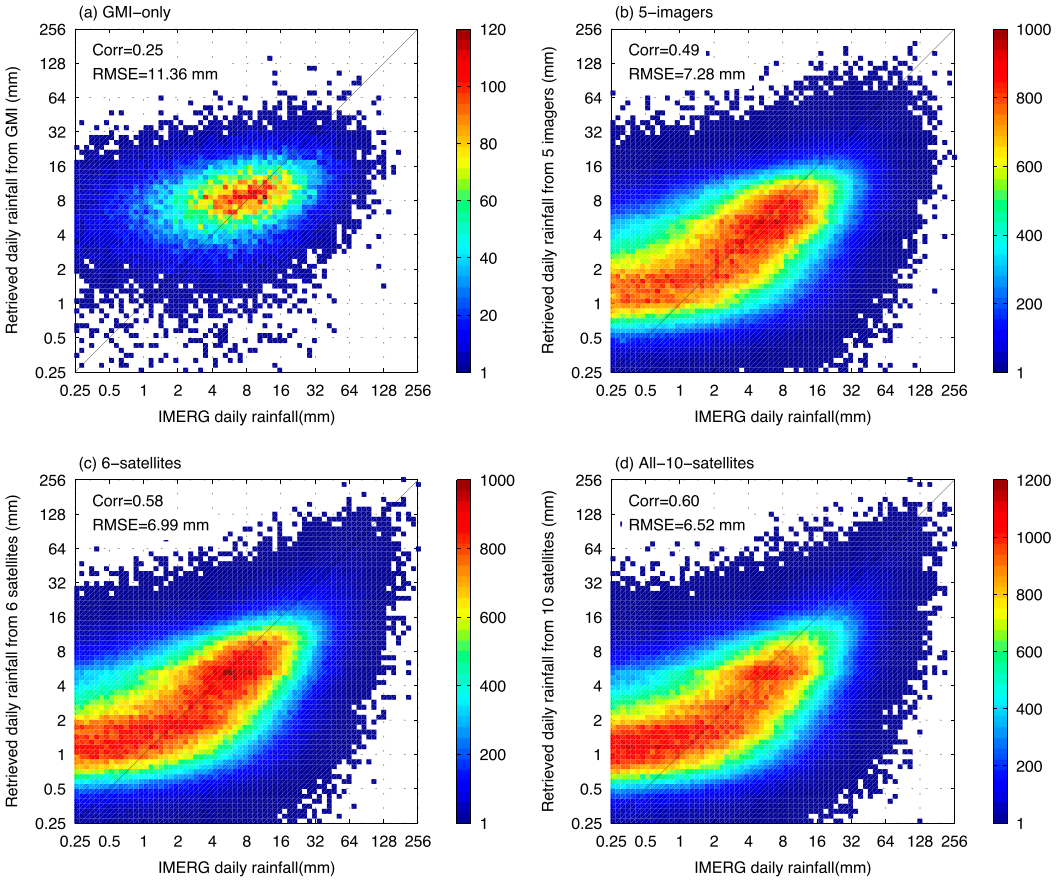

FIG. 10. (a) Density scatterplot between IMERG daily rainfall amount and retrieved daily rainfall amount based on the emissivity temporal variation (Δe) at 19, 24, and 37 GHz, derived from GMI observations only. (b) As in (a), but the Δe is derived from five imagers, including GMI, AMSR2, and three SSMIS. (c) As in (a), but the Δe is derived from six sensors, including GMI and five other radiometers on board the sun-synchronous satellites (i.e., AMSR2 on board *GCOM-W1*, AMSU-A on board *NOAA-19*, SSMIS on board *F16* and *F17*, and AMSU-A on board *MetOp-A*). These five sensors have very different equator crossing time, as shown in Fig. 9. (d) As in (a), but the Δe is derived from all 10 satellites.

nonraining background in the preceding day when using five imagers for over 85% of the time. In contrast, only about 34% of the time one can find a nonraining background when only GMI observations are used. For the majority of the time, the nonraining background is 2, 3, or even more days away when only GMI is used. With the longer time difference, it is more likely that the emissivity varies due to factors other than the rainfall impact, or the rainfall effect might be missed. Second, with more observations from five satellites, the diurnal cycle of the emissivity can be much better captured than that using GMI observations only. In fact, on average, the daily sample size over each 0.5° grid box is 10 when using 5 imagers, while it is only 1 or 2 from GMI. Lin and Minnis (2000) found that the emissivity of 19 GHz from Special Sensor Microwave Imager (SSM/I) at the early morning (0640 local time) is about 0.06 less than that at other times over a Southern Great Plains site, and they concluded that dew and surface rewetting effects may be responsible for the emissivity diurnal cycle. The large emissivity discrepancy between daytime and nighttime (up to 0.1 over some arid regions) has also been noticed by Norouzi et al. (2012) using AMSR-E observations, although they pointed out that the different diurnal cycles between the skin temperature and the soil temperature are responsible for the large emissivity discrepancy. Regardless of the underlying mechanisms causing the emissivity diurnal cycle, more observations from multiple satellites can better capture the daily emissivity variation compared with those from a single satellite. Third, the increased temporal sampling from multiple satellites provides a better chance of an observation right after the rainfall has ended, when its effect on emissivity is maximum.

By carefully selecting six sensors with much different ECTs, the retrieval performance is further improved, indicated by the correlation being 0.58 and RMSE being 6.99 mm (Fig. 10c). The time difference between using five imagers and using six sensors is similar (Fig. 11). That is, over 85% of the time difference in both experiments is one day. However, with the much variable ECTs from the 6-satellites scheme, the emissivity variation can be better captured than that in the 5-imagers

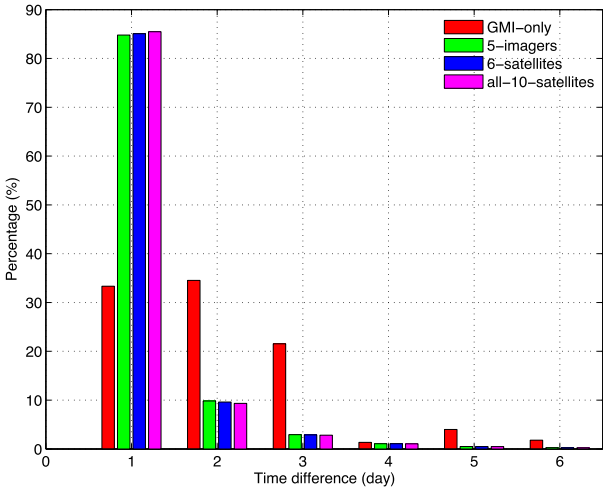

FIG. 11. The time difference between raining day and nonraining day (background), as defined in Eq. (2), for all four retrieval experiments shown in Fig. 10.

scheme. As mentioned previously, ECTs from F17 and F18 are very similar from 2014 to 2018 (Fig. 9). By using observations from all-10-satellites scheme, the retrieval results only improve marginally with the correlation being 0.60 and RMSE being 6.52 mm, compared with that from the 6-satellites scheme. The marginal improvement is expected since ECTs from several satellite are similar (Fig. 9; *MetOp-A* and *MetOp-B*, *F17*, *F18* and *NOAA-18*, AMSR2 and ATMS). This means that observations from these satellites with similar ECTs add little new information.

A common feature in the retrieval result from Figs. 10b–d is that for rain rates less than 1 mm, the retrieval algorithm has little skill. This phenomenon may reflect the fact that the soil moisture has little response for daily rainfall accumulations less than 1 mm.

4. Conclusions and discussions

This study presents a rainfall retrieval algorithm to estimate the daily rainfall accumulation from nonraining satellite observations from 10 satellites, including GMI, AMSR2, SSMIS on board *F16*, *F17*, and *F18* satellites, ATMS on board *SNPP* satellite, and AMSU-A on board *NOAA-18*, *NOAA-19*, *MetOp-A*, and *MetOp-B* satellites. In contrast to the traditionally used ice-scattering signal over land, we use the land surface emissivity variation signature due to the rainfall impact for rainfall retrieval by filtering out the raining pixels. To compute the emissivity temporal variation, we first convert frequencies from other sensors to GMI frequencies from 19 (or 24) to 89 GHz. Results show that RMSE is less than 3 K over the vast majority of the regions for all nine sensors and for all channels, leading to about 0.01 emissivity uncertainty.

The objective of this study is to use the nonraining pixels to compute the emissivity. To this end, we need to filter out the raining pixels first. Our statistical method shows strong capability to detect raining pixel, indicating by POD and HSS greater than 0.70 over the majority of the region. The rainfall retrieval algorithm is only applied to the rainfall-sensitive region, defined as the areas where the land surface emissivity drops at least 0.02 at H19 corresponding to the previous 1-day rainfall accumulation greater than 20 mm.

While the best rainfall retrieval performance is achieved by using observations from all-10-satellites scheme, with the correlation and RMSE being 0.60 and 6.52 mm, analysis shows that by selecting GMI and five sensors on board the sun-synchronous satellites with much different ECTs (i.e., 6-satellites scheme), the retrieval performance is comparable to that from 10 satellites, as indicated by the correlation of 0.58 and RMSE of 6.99 mm. In contrast, the retrieval results from the 5-imagers scheme are noticeably worse than those 6-satellites and all-10-satellites schemes because the emissivity variation can be much better captured by using all 10 satellites or six satellites with much different ECTs, compared with only using five imagers. Furthermore, there is low retrieval skill when only the GMI observations are used due to the much smaller sample size, which leads to a longer time difference between the raining day and the nonraining day. Also, it is not possible to capture the emissivity diurnal cycle with GMI observations only.

Future work seeks to further include the currently operational radiometers, including ATMS on board *NOAA-20*, AMSU-A on board *MetOp-C*, WindSat, and *FengYun-3* Microwave Radiometer Imager (MWRI). With more observations, the retrieval performance from our method is expected to be further improved. In particular, we expect a large retrieval performance improvement when the passive microwave radiometer observations around 0800 and 1100 local time are available (see Fig. 9) in the future.

Acknowledgments. GMI, AMSR2, SSMIS, ATMS, and IMERG data are downloaded from NASA Precipitation Processing System (PPS) website (https://storm.pps.eosdis.nasa.gov/storm/). AMSU-A data are downloaded from NOAA (https://www.ncdc.noaa.gov/cdr/fundamental/amsu-brightness-temperature). This work is supported by NASA's Precipitation Measurement Missions Program science team under the management of Dr. Gail Skofronick-Jackson via the Internal Scientist Funding Model, and the NASA Grant 80NSSC20K0903 from the Weather and Atmospheric Dynamics program. Y.Y also would like to acknowledge the financial support from NOAA Grant NA19NES4320002 (Cooperative Institute for Satellite Earth System Studies-CISESS) at the University of Maryland/ESSIC.

REFERENCES

Aires, F., C. Prigent, F. Bernardo, C. Jiménez, R. Saunders, and P. Brunel, 2011: A Tool to Estimate Land-Surface Emissivities at Microwave frequencies (TELSEM) for use in numerical weather prediction. *Quart. J. Roy. Meteor. Soc.*, **137**, 690–699, https://doi.org/10.1002/qj.803.

Aonashi, K., and Coauthors, 2009: GSMaP passive microwave precipitation retrieval algorithm: Algorithm description and validation. *J. Meteor. Soc. Japan*, **87A**, 119–136, https://doi.org/10.2151/jmsj.87A.119.

Birman, C., F. Karbou, and J.-F. Mahfouf, 2015: Daily rainfall detection and estimation over land using microwave surface

emissivities. *J. Appl. Meteor. Climatol.*, **54**, 880–895, https://doi.org/10.1175/JAMC-D-14-0192.1.

Boukabara, S.-A., and Coauthors, 2011: MiRS: An all-weather 1DVAR satellite data assimilation and retrieval system. *IEEE Trans. Geosci. Remote Sens.*, **49**, 3249–3272, https://doi.org/10.1109/TGRS.2011.2158438.

Brocca, L., and Coauthors, 2014: Soil as a natural rain gauge: Estimating global rainfall from satellite soil moisture data. *J. Geophys. Res. Atmos.*, **119**, 5128–5141, https://doi.org/10.1002/2014JD021489.

Chiu, J. C., and G. W. Petty, 2006: Bayesian retrieval of complete posterior PDFs of oceanic rain rate from microwave observations. *J. Appl. Meteor. Climatol.*, **45**, 1073–1095, https://doi.org/10.1175/JAM2392.1.

Crow, W. T., G. J. Huffman, R. Bindlish, and T. J. Jackson, 2009: Improving satellite-based rainfall accumulation estimates using spaceborne surface soil moisture retrievals. *J. Hydrometeor.*, **10**, 199–212, https://doi.org/10.1175/2008JHM986.1.

Ebtehaj, A. M., R. L. Bras, and E. Foufoula-Georgiou, 2015: Shrunken locally linear embedding for passive microwave retrieval of precipitation. *IEEE Trans. Geosci. Remote Sens.*, **53**, 3720–3736, https://doi.org/10.1109/TGRS.2014.2382436.

Evans, K. F., J. Turk, T. Wong, and G. L. Stephens, 1995: A Bayesian approach to microwave precipitation profile retrieval. *J. Appl. Meteor.*, **34**, 260–279, https://doi.org/10.1175/1520-0450-34.1.260.

Ferraro, R. R., and G. F. Marks, 1995: The development of SSM/I rain-rate retrieval algorithms using ground-based radar measurements. *J. Atmos. Oceanic Technol.*, **12**, 755–770, https://doi.org/10.1175/1520-0426(1995)012<0755:TDOSRR>2.0.CO;2.

——, N. C. Grody, and G. F. Marks, 1994: Effects of surface conditions on rain identification using the DMSP-SSM/I. *Remote Sens. Rev.*, **11**, 195–209, https://doi.org/10.1080/02757259409532265.

——, F. Weng, N. C. Grody, and L. Zhao, 2000: Precipitation characteristics over land from the NOAA-15 AMSU sensor. *Geophys. Res. Lett.*, **27**, 2669–2672, https://doi.org/10.1029/2000GL011665.

——, and Coauthors, 2013: An evaluation of microwave land surface emissivities over the continental United States to benefit GPM-era precipitation algorithms. *IEEE Trans. Geosci. Remote Sens.*, **51**, 378–398, https://doi.org/10.1109/TGRS.2012.2199121.

Gelaro, R., and Coauthors, 2017: The Modern-Era Retrospective Analysis for Research and Applications, version 2 (MERRA-2). *J. Climate*, **30**, 5419–5454, https://doi.org/10.1175/JCLI-D-16-0758.1.

Gopalan, K., N.-Y. Wang, R. Ferraro, and C. Liu, 2010: Status of the TRMM 2A12 land precipitation algorithm. *J. Atmos. Oceanic Technol.*, **27**, 1343–1354, https://doi.org/10.1175/2010JTECHA1454.1.

Grody, N. C., 1991: Classification of snow cover and precipitation using the special sensor microwave imager. *J. Geophys. Res.*, **96**, 7423–7435, https://doi.org/10.1029/91JD00045.

Huffman, G. J., D. T. Bolvin, D. Braithwaite, K. Hsu, R. Joyce, C. Kidd, E. J. Nelkin, and P. Xie, 2015: NASA Global Precipitation Measurement Integrated Multi-satellitE Retrievals for GPM (IMERG). Algorithm Theoretical Basis Doc., version 4.5, 30 pp., http://pmm.nasa.gov/sites/default/files/document_files/IMERG_ATBD_V4.5.pdf.

Islam, T., P. K. Srivastava, M. A. Rico-Ramirez, Q. Dai, D. Han, and M. Gupta, 2014: An exploratory investigation of an Adaptive Neuro Fuzzy Inference System (ANFIS) for estimating hydrometeors from TRMM/TMI in synergy with TRMM/PR. *Atmos. Res.*, **145–146**, 57–68, https://doi.org/10.1016/j.atmosres.2014.03.019.

Jackson, T. J., 1993: III. Measuring surface soil moisture using passive microwave remote sensing. *Hydrol. Processes*, **7**, 139–152, https://doi.org/10.1002/hyp.3360070205.

Kim, M.-J., J. Weinman, W. Olson, D.-E. Chang, G. Skofronick-Jackson, and J. Wang, 2008: A physical model to estimate snowfall over land using AMSU-B observations. *J. Geophys. Res.*, **113**, D09201, https://doi.org/10.1029/2007JD008589.

Koster, R. D., L. Brocca, W. T. Crow, M. S. Burgin, and G. J. De Lannoy, 2016: Precipitation estimation using L-band and C-band soil moisture retrievals. *Water Resour. Res.*, **52**, 7213–7225, https://doi.org/10.1002/2016WR019024.

Kubota, T., and Coauthors, 2007: Global precipitation map using satellite-borne microwave radiometers by the GSMaP Project: Production and validation. *IEEE Trans. Geosci. Remote Sens.*, **45**, 2259–2275, https://doi.org/10.1109/TGRS.2007.895337.

Kummerow, C. D., W. S. Olson, and L. Giglio, 1996: A simplified scheme for obtaining precipitation and vertical hydrometeor profiles from passive microwave sensors. *IEEE Trans. Geosci. Remote Sens.*, **34**, 1213–1232, https://doi.org/10.1109/36.536538.

——, D. L. Randel, M. Kulie, N.-Y. Wang, R. Ferraro, S. Joseph Munchak, and V. Petkovic, 2015: The evolution of the Goddard profiling algorithm to a fully parametric scheme. *J. Atmos. Oceanic Technol.*, **32**, 2265–2280, https://doi.org/10.1175/JTECH-D-15-0039.1.

Lin, B., and P. Minnis, 2000: Temporal variations of land surface microwave emissivities over the Atmospheric Radiation Measurement program Southern Great Plains site. *J. Appl. Meteor.*, **39**, 1103–1116, https://doi.org/10.1175/1520-0450(2000)039<1103:TVOLSM>2.0.CO;2.

McColl, K. A., S. H. Alemohammad, R. Akbar, A. G. Konings, S. Yueh, and D. Entekhabi, 2017: The global distribution and dynamics of surface soil moisture. *Nat. Geosci.*, **10**, 100–104, https://doi.org/10.1038/ngeo2868.

Meng, H., J. Dong, R. Ferraro, B. Yan, L. Zhao, C. Kongoli, N.-Y. Wang, and B. Zavodsky, 2017: A 1DVAR-based snowfall rate retrieval algorithm for passive microwave radiometers. *J. Geophys. Res. Atmos.*, **122**, 6520–6540, https://doi.org/10.1002/2016JD026325.

Munchak, S. J., S. Ringerud, L. Brucker, Y. You, I. de Gelis, and C. Prigent, 2020: An active-passive microwave land surface database from GPM. *IEEE Trans. Geosci. Remote Sens.*, **58**, 6224–6242, https://doi.org/10.1109/TGRS.2020.2975477.

Noh, Y.-J., G. Liu, E.-K. Seo, J. R. Wang, and K. Aonashi, 2006: Development of a snowfall retrieval algorithm at high microwave frequencies. *J. Geophys. Res.*, **111**, D22216, https://doi.org/10.1029/2005JD006826.

Norouzi, H., W. Rossow, M. Temimi, C. Prigent, M. Azarderakhsh, S. Boukabara, and R. Khanbilvardi, 2012: Using microwave brightness temperature diurnal cycle to improve emissivity retrievals over land. *Remote Sens. Environ.*, **123**, 470–482, https://doi.org/10.1016/j.rse.2012.04.015.

Pellarin, T., S. Louvet, C. Gruhier, G. Quantin, and C. Legout, 2013: A simple and effective method for correcting soil moisture and precipitation estimates using AMSR-E measurements. *Remote Sens. Environ.*, **136**, 28–36, https://doi.org/10.1016/j.rse.2013.04.011.

Petty, G. W., and K. Li, 2013a: Improved passive microwave retrievals of rain rate over land and ocean. Part I: Algorithm description. *J. Atmos. Oceanic Technol.*, **30**, 2493–2508, https://doi.org/10.1175/JTECH-D-12-00144.1.

——, and ——, 2013b: Improved passive microwave retrievals of rain rate over land and Ocean. Part II: Validation and intercomparison. *J. Atmos. Oceanic Technol.*, **30**, 2509–2526, https://doi.org/10.1175/JTECH-D-12-00184.1.

Prigent, C., F. Aires, and W. Rossow, 2006: Land surface microwave emissivities over the globe for a decade. *Bull. Amer. Meteor. Soc.*, **87**, 1573–1584, https://doi.org/10.1175/BAMS-87-11-1573.

Romanov, P., 2017: Global Multisensor Automated satellite-based Snow and Ice Mapping System (GMASI) for cryosphere monitoring. *Remote Sens. Environ.*, **196**, 42–55, https://doi.org/10.1016/j.rse.2017.04.023.

Sano, P., D. Casella, A. Mugnai, G. Schiavon, E. A. Smith, and G. J. Tripoli, 2013: Transitioning from CRD to CDRD in Bayesian retrieval of rainfall from satellite passive microwave measurements: Part 1. Algorithm description and testing. *IEEE Trans. Geosci. Remote Sens.*, **51**, 4119–4143, https://doi.org/10.1109/TGRS.2012.2227332.

Shige, S., and Coauthors, 2009: The GSMaP precipitation retrieval algorithm for microwave sounders—Part I: Over-ocean algorithm. *IEEE Trans. Geosci. Remote Sens.*, **47**, 3084–3097, https://doi.org/10.1109/TGRS.2009.2019954.

Spencer, R., D. Martin, B. Hinton, and J. Weinman, 1983a: Satellite microwave radiances correlated with radar rain rates over land. *Nature*, **304**, 141–143, https://doi.org/10.1038/304141a0.

——, W. Olson, W. Rongzhang, D. Martin, J. Weinman, and D. Santek, 1983b: Heavy thunderstorms observed over land by the Nimbus 7 Scanning Multichannel Microwave Radiometer. *J. Climate Appl. Meteor.*, **22**, 1041–1046, https://doi.org/10.1175/1520-0450(1983)022<1041:HTOOLB>2.0.CO;2.

Spencer, R. W., H. M. Goodman, and R. E. Hood, 1989: Precipitation retrieval over land and ocean with the SSM/I: Identification and characteristics of the scattering signal. *J. Atmos. Oceanic Technol.*, **6**, 254–273, https://doi.org/10.1175/1520-0426(1989)006<0254:PROLAO>2.0.CO;2.

Staelin, D. H., and F. W. Chen, 2000: Precipitation observations near 54 and 183 GHz using the NOAA-15 satellite. *IEEE Trans. Geosci. Remote Sens.*, **38**, 2322–2332, https://doi.org/10.1109/36.868889.

Surussavadee, C., and D. H. Staelin, 2010: NPOESS precipitation retrievals using the ATMS passive microwave spectrometer. *IEEE Geosci. Remote Sens. Lett.*, **7**, 440–444, https://doi.org/10.1109/LGRS.2009.2038614.

Turk, F. J., Z. S. Haddad, and Y. You, 2014: Principal components of multifrequency microwave land surface emissivities. Part I: Estimation under clear and precipitating conditions. *J. Hydrometeor.*, **15**, 3–19, https://doi.org/10.1175/JHM-D-13-08.1.

Wang, N.-Y., C. Liu, R. Ferraro, D. Wolff, E. Zipser, and C. Kummerow, 2009: TRMM 2A12 land precipitation product-status and future plans. *J. Meteor. Soc. Japan*, **87A**, 237–253, https://doi.org/10.2151/jmsj.87A.237.

Wilks, D. S., 2011: *Statistical Methods in the Atmospheric Sciences*. 3rd ed. International Geophysics Series, Vol. 100, Academic Press, 704 pp.

Xie, P., R. Joyce, S. Wu, S.-H. Yoo, Y. Yarosh, F. Sun, and R. Lin, 2017: Reprocessed, bias-corrected CMORPH global high-resolution precipitation estimates from 1998. *J. Hydrometeor.*, **18**, 1617–1641, https://doi.org/10.1175/JHM-D-16-0168.1.

Yang, S., F. Weng, B. Yan, N. Sun, and M. Goldberg, 2011: Special Sensor Microwave Imager (SSM/I) intersensor calibration using a simultaneous conical overpass technique. *J. Appl. Meteor. Climatol.*, **50**, 77–95, https://doi.org/10.1175/2010JAMC2271.1.

——, J. Hawkins, and K. Richardson, 2014: The improved NRL tropical cyclone monitoring system with a unified microwave brightness temperature calibration scheme. *Radio Sci.*, **6**, 4563–4581, https://doi.org/10.3390/rs6054563.

Yin, J., X. Zhan, J. Liu, and M. Schull, 2019: An intercomparison of Noah model skills with benefits of assimilating SMOPS blended and individual soil moisture retrievals. *Water Resour. Res.*, **55**, 2572–2592, https://doi.org/10.1029/2018WR024326.

You, Y., F. J. Turk, Z. S. Haddad, L. Li, and G. Liu, 2014: Principal components of multifrequency microwave land surface emissivities. Part II: Effects of previous-time precipitation. *J. Hydrometeor.*, **15**, 20–37, https://doi.org/10.1175/JHM-D-13-07.1.

——, N.-Y. Wang, and R. Ferraro, 2015: A prototype precipitation retrieval algorithm over land using passive microwave observations stratified by surface condition and precipitation vertical structure. *J. Geophys. Res. Atmos.*, **120**, 5295–5315, https://doi.org/10.1002/2014JD022534.

——, ——, ——, and P. Meyers, 2016: A prototype precipitation retrieval algorithm over land for ATMS. *J. Hydrometeor.*, **17**, 1601–1621, https://doi.org/10.1175/JHM-D-15-0163.1.

——, C. Peters-Lidard, J. Turk, S. Ringerud, and S. Yang, 2017: Improving overland precipitation retrieval with brightness temperature temporal variation. *J. Hydrometeor.*, **18**, 2355–2383, https://doi.org/10.1175/JHM-D-17-0050.1.

——, ——, N.-Y. Wang, J. Turk, S. Ringerud, S. Yang, and R. Ferraro, 2018: The instantaneous retrieval of precipitation over land by temporal variation at 19 GHz. *J. Geophys. Res. Atmos.*, **123**, 9279–9295, https://doi.org/10.1029/2017JD027596.

——, and Coauthors, 2020: Comparison of TRMM microwave imager rainfall datasets from NASA and JAXA. *J. Hydrometeor.*, **21**, 377–397, https://doi.org/10.1175/JHM-D-19-0022.1.